Journal of Materials Chemistry A

Accepted Manuscript

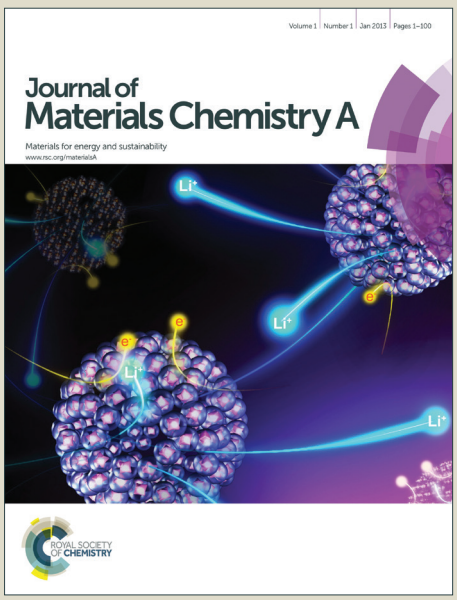

ROYAL SOCIETY OF CHEMISTRY

www.rsc.org/materialsA

Journal Name RSCPublishing

ARTICLE

Novel heterojunction photocatalyst based on lanthanum titanate nanosheets and indium oxide nanoparticles with enhanced photocatalytic hydrogen production activity

Cite this: DOI: 10.1039/x0xx00000x

Received 00th January 2014,
Accepted 00th January 2014

DOI: 10.1039/x0xx00000x

www.rsc.org/

Sujuan Hu, Bo Chi,* Jian Pu and Li Jian

A lanthanum titanate ($La_2Ti_2O_7$) and indium oxide (In_2O_3) heterojunction nanocomposite is synthesized by a solvothermal method. The crystal phase, morphology, optical absorption activity and chemical composition of the $In_2O_3/La_2Ti_2O_7$ heterojunction nanocomposites are characterized by X-ray diffraction, scanning electron microscopy, transmission electron microscopy, UV-Vis diffuse reflectance spectra and X-ray photoelectron spectroscopy. The results reveal that In_2O_3 nanoparticles are uniformly dispersed on $La_2Ti_2O_7$ nanosheets surfaces with good adhesion. The $In_2O_3/La_2Ti_2O_7$ nanocomposite with a molar ratio of 1.5:1 exhibits the highest H_2 production rate when used in photocatalytic water splitting, as improved by 29.62 and 6.43 times relative to pure In_2O_3 and $La_2Ti_2O_7$, respectively. The enhanced photocatalytic H_2 production rate can be ascribed to the formation of the heterojunction structure that results from the homogeneous dispersion of In_2O_3 nanoparticles on $La_2Ti_2O_7$ nanosheets. The configuration of the $In_2O_3/La_2Ti_2O_7$ heterojunction nanocomposite photocatalyst can promote the fast separation of photogenerated carriers in space and improve the rate of water-splitting to form H_2.

1. Introduction

With the depletion of fossil fuel reserves and the subsequent need for sustainable energy sources, hydrogen as a clean and renewable energy source has become a favored fuel for supplanting conventional fossil fuel-derived-energy.[1-5] Since Fujishima and Honda first reported the photoelectrochemical splitting of water into H_2 and O_2 on a TiO_2 semiconductor electrode, various photocatalytic water-splitting semiconductors for solar-driven H_2 production have been studied.[6-10] Among these semiconductors, (110) layered-structure perovskites, such as $M_2N_2O_7$ (M = Ca, Sr, La; N = Nb, Ti), have received increasing attention because of their unique electronic configuration, high chemical resistance and interlayer spatial structure, enabling the use of different reaction sites for water oxidation and reduction.[11, 12] Among the perovskites, lanthanum titanate ($La_2Ti_2O_7$, LTO) has received major attention because of its efficiency in photocatalytic H_2 production from water splitting.[13-16] The conventional preparation methods of $La_2Ti_2O_7$ are via solid-state reaction (SSR) and sol-gel methods. However, neither of these methods is convenient or economical. In addition, the particles obtained are large with undesirably low specific surface areas.[13, 14] These characteristics are not favourable to efficient and low-cost photocatalytic H_2 production activity.

Furthermore, the high recombination rate of photogenerated electron-hole pairs in $La_2Ti_2O_7$ restricts the enhancement of its photocatalytic H_2 production activity. Hence, the modulation of photogenerated charge carrier transformation in $La_2Ti_2O_7$ is crucial to enhancing the photoconversion efficiency of solar energy. One proposed and effective means of modulating carrier transformation is through the use of a heterojunction structure or coupling two semiconductor units with appropriate band alignment between the two units to allow interfacial charge transfer upon excitation and promote the separation efficiency of photogenerated electrons and holes.[17-19] For example, Qian and coworkers found that novel $Bi_2S_3/Bi_2O_2CO_3$ heterojunction photocatalysts showed greatly improved photoactivity compared to that of pure $Bi_2O_2CO_3$.[18] The enhancement was ascribed to the improved dispersion of Bi_2S_3 on the $Bi_2O_2CO_3$ nanoparticle surfaces and the more intimate $Bi_2S_3/Bi_2O_2CO_3$ heterojunction structure. Zhou et al. reported single n-ZnO/p-AlGaN heterojunction nanowires with excellent optoelectronic properties. The formation of a high-quality interfacial structure enhanced the excitation efficiency in the interfacial layer between ZnO and AlGaN.[20]

In_2O_3 is a well-known semiconductor with an indirect bandgap of 2.8 eV. It has been demonstrated to be an efficient sensitizer for extending the absorption region from UV to the visible-light range.[21, 22] Because the conduction band (CB) and valance band (VB) positions of $La_2Ti_2O_7$ (-0.43 eV and 3.37 eV, respectively, vs. NHE) are both higher than those of In_2O_3 (-0.63 eV and 2.17 eV, respectively, vs. NHE), the use of an $In_2O_3/La_2Ti_2O_7$ heterojunction would result in an improvement in the efficient separation of photogenerated charge carriers. In such an $In_2O_3/La_2Ti_2O_7$ heterojunction structure, the coupling of $La_2Ti_2O_7$ with In_2O_3 creates an electrostatic field opposite to the built-in potential, which can improve the separation efficiency of photogenerated electron-hole pairs.[23-25] To be specific, the accumulated photogenerated electrons of In_2O_3 are readily trapped by a co-catalyst, such as Pt, Ag or NiO_x, to reduce water to hydrogen. The accumulated photogenerated holes in $La_2Ti_2O_7$ are subsequently oxidized by a sacrifice reagent.

For a photocatalyst to be efficient, a large specific surface area is desirable. To obtain such an area for the catalysts reported in this work, a hydrothermal method was used to prepare two-dimensional $La_2Ti_2O_7$ nanosheets because this morphology is more effective than zero-dimensional $La_2Ti_2O_7$ particles from the viewpoint of the mobility and recombination rate of charge carriers.[15, 16, 26] Few studies have been conducted on $La_2Ti_2O_7$ nanosheet-based heterojunction photocatalysts. Here, we have used a solvothermal method to prepare $In_2O_3/La_2Ti_2O_7$ heterojunction photocatalysts to investigate the synergistic effects of the In_2O_3 and $La_2Ti_2O_7$ combination on the photocatalytic H_2 production activity. The as-prepared $In_2O_3/La_2Ti_2O_7$ heterojunction nanocomposite with the optimal molar ratio of 1.5:1 shows much higher H_2 production activity and higher stability than the other materials tested under water-splitting conditions. The enhanced photocatalytic activity can be attributed not only to the large specific surface area of $La_2Ti_2O_7$ and the enhancement of visible light absorption by In_2O_3 but also can be ascribed to the more effective separation of photogenerated carriers that is driven by the electrostatic field in the $In_2O_3/La_2Ti_2O_7$ heterojunction structure.

2. Experimental

2.1 Materials

All chemicals were of analytical grade and purchased from Sinopharm Chemical Reagent Co., Ltd. without further purification before use. High-purity deionized (DI) water was used throughout the experiments.

2.2 Preparation

$La_2Ti_2O_7$ nanosheets were prepared by a hydrothermal method.[15] Specifically, 5 mmol $Ti(OBu)_4$ was mixed in 50 mmol CH_3COOH while stirring vigorously for 30 min and 5 mmol $La(NO_3)_3 \cdot 6H_2O$ was dissolved in 10 mL deionized water. This was added dropwise to the $Ti(OBu)_4/CH_3COOH$ mixture, giving a clear aqueous solution. 30 mL 1.8 M NaOH solution was then added to this solution. The resulting solution was transferred to a 100 mL Teflon-lined stainless steel autoclave and heat-treated at 200 °C for 24 h. The product was collected after centrifugation, washed with water and ethanol repeatedly, and then dried at 80 °C for 12 h.

To form the $In_2O_3/La_2Ti_2O_7$ heterojunction, In_2O_3 nanocrystals were grown in situ on $La_2Ti_2O_7$ nanosheets. A mixture of 0.8 mmol $In(NO_3)_3 \cdot 5H_2O$, 0.8 mmol $La_2Ti_2O_7$, 1 mL formamide and 2.4 mmol sodium dodecylbenzene sulfonate (SDBS) in 48 mL anhydrous ethanol was vigorously stirred magnetically for 1 h. The resulting precipitate was transferred into a 100 mL Teflon-lined stainless steel autoclave and heat-treated at 160 °C for 24 h. The precipitate was washed again and further annealed at 500 °C for 2 h to obtain an $In_2O_3/La_2Ti_2O_7$ nanocomposite photocatalyst. A series of $In_2O_3/La_2Ti_2O_7$ nanocomposite photocatalysts with different molar ratios (2:1, 1.5:1, 1:1, 0.5:1 and 0.25:1) were synthesized in a similar fashion by adjusting the amount of $In(NO_3)_3 \cdot 5H_2O$ added. A pure In_2O_3 control catalyst was also synthesized following the same procedure in the absence of $La_2Ti_2O_7$.

Deposition of Pt (1.0 wt%) co-catalyst on a $La_2Ti_2O_7$ surface was achieved through typical in-situ photoreduction of H_2PtCl_6 with UV-light irradiation.[27] One gram of the photocatalyst powder was suspended in 200 ml of aqueous solution containing 20 %(v/v) methanol as the sacrificial donor. 0.0265g of $H_2PtCl_6 \cdot 6H_2O$ was added to the mixture. Following this, the suspension was stirred and purged with N_2 continually to ensure anaerobic conditions. After that, the suspension was illuminated with UV light for 4 h. The precipitate was collected by centrifugation and dried at 80 ºC for 12 h.

2.3 Characterization

X-ray diffraction (XRD) measurements were carried out using an X-ray diffractometer (XRD, X'Pert pro. PANalytical B.V) with Cu Kα radiation. Both scanning electron microscopy (FE-SEM, FEI, Sirion 200) and transmission electron microscopy (TEM, JEM-2100F) were used to characterize the morphologies of the samples. X-ray photoelectron spectroscopy (XPS) was performed on a KRATOS AXIS165 X-ray photoelectron spectrometer. The UV-Vis diffuse reflectance spectra were recorded with a Perkin-Elmer Lambda 35 UV-Vis spectrophotometer. Photoluminescence (PL) spectra were measured using laser confocal Raman microspectroscopy (LabRAM HR800, Horiba JobinYvon) with an excitation wavelength of 325 nm.

2.4 Photocatalytic activity

The photocatalytic H_2 production experiments were performed in a quartz reactor under solar light irradiation at ambient temperature and atmospheric pressure. A 500 W Xe lamp (100 mW cm^{-2}, CHF-XM 500, Beijing Trusttech Co., Ltd.) was used as the simulated solar light source. In a typical photocatalytic experiment, 0.1 g photocatalyst powder was suspended in 150 ml aqueous solution containing 25 %(v/v) methanol. Before photocatalytic H_2 production experiments, the reaction vessel was evacuated for 30 min to remove dissolved oxygen and ensure anaerobic conditions. Throughout the experiment 1 mL of gas was sampled intermittently and hydrogen content was analyzed using a gas chromatograph (DongXi GC-A5000, with high purity Ar carrier gas) equipped with a thermal conductivity detector. The apparent quantum efficiency (AQE)

was measured under the same photocatalytic reaction conditions. The focused intensity and areas on the flask for Xe lamp was ca. 100 mW cm^{-2} and 19 cm^2, respectively. The AQE can be calculated according to the following equation:

$$\text{AQE [\%]} = \frac{\text{number of reacted electrons}}{\text{number of incident photons}} \times 100$$
$$= \frac{\text{number of evolved } H_2 \text{ molecules} \times 2}{\text{number of incident photons}} \times 100$$

2.5 Photo-electrochemical measurement

Photocurrents and Mott–Schottky plots were measured using an electrochemical analyzer (Zennium, Zahner) with a standard three-electrode system using the prepared samples as the working electrodes, a platinum plate as the counter electrode, and a Ag/AgCl (saturated KCl) electrode as the reference electrode in 1 M Na_2SO_4 aqueous solution. A 500 W Xe lamp (100 mW cm^{-2}, CHF-XM 500, Beijing Trusttech Co., Ltd.) was used as the light source. For the preparation of the working electrodes, 0.2 g of the photocatalyst was ground with 0.06 g polyethylene glycol (PEG, molecular weight: 20000 Da) and 0.5 mL water to make a slurry. The slurry was subsequently coated onto a 2 cm×1.5 cm FTO glass electrode by the doctor-blade method. The resulting electrodes were dried and calcined at 450 ºC for 30 min. All electrodes studied had a similar film thickness (10~11 μm).[28, 29]

3. Results and Discussion

3.1. Crystal phase analysis

The XRD patterns of In_2O_3, $La_2Ti_2O_7$ and $In_2O_3/La_2Ti_2O_7$ nanocomposites with different molar ratios are shown in Fig. 1. It can be found that pure $La_2Ti_2O_7$ prepared by a hydrothermal method shows a monoclinic phase with a perovskite structure belonging to the $P2_1$ space group (JCPDS 81-1066). After forming a composite of $La_2Ti_2O_7$ with In_2O_3 by solvothermal treatment at 160 ºC for 24 h, additional diffraction peaks with 2θ = 30.48, 35.44, 45.71, 51.03, and 60.80º appear, which can be indexed to the (222), (400), (431), (440), and (622) crystal planes of the body-centered cubic In_2O_3 crystalline phase (JCPDS 71-2194). No characteristic peaks for any impurities, such as In, $In(OH)_3$ or $InTiO_5$, can be observed, suggesting that the composition of the photocatalyst is exclusively In_2O_3 and $La_2Ti_2O_7$.

3.2. Morphology and microstructure analysis

Typical SEM images of In_2O_3, $La_2Ti_2O_7$ and the $In_2O_3/La_2Ti_2O_7$ nanocomposite with a molar ratio of 1.5:1 are shown in Fig. 2. As seen from Fig. 2A and 2B, In_2O_3 shows aggregated spherical nanoparticles with coarse surfaces that fall within the narrow size range of 40 to 60 nm (Fig. 2A), while pure $La_2Ti_2O_7$ shows irregular well-dispersed thin nanosheets (Fig. 2B). The $In_2O_3/La_2Ti_2O_7$ nanocomposite with a molar ratio of 1.5:1 (Fig. 2C and 2D) exhibits a homogeneous dispersion of In_2O_3 spherical nanoparticles upon the $La_2Ti_2O_7$ nanosheets with good adhesion. No obvious aggregate formation is observed.

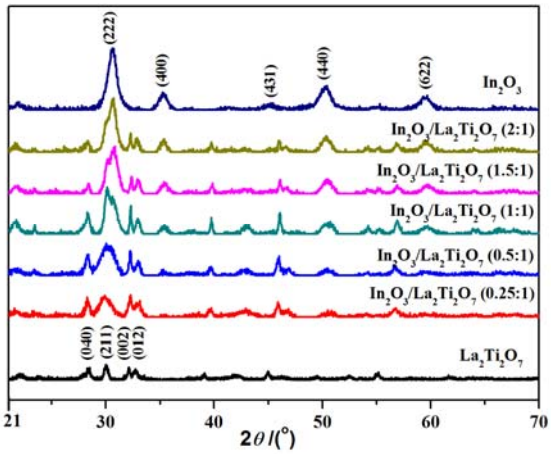

Fig. 1 XRD patterns of In_2O_3, $La_2Ti_2O_7$ and $In_2O_3/La_2Ti_2O_7$ nanocomposites with different molar ratios.

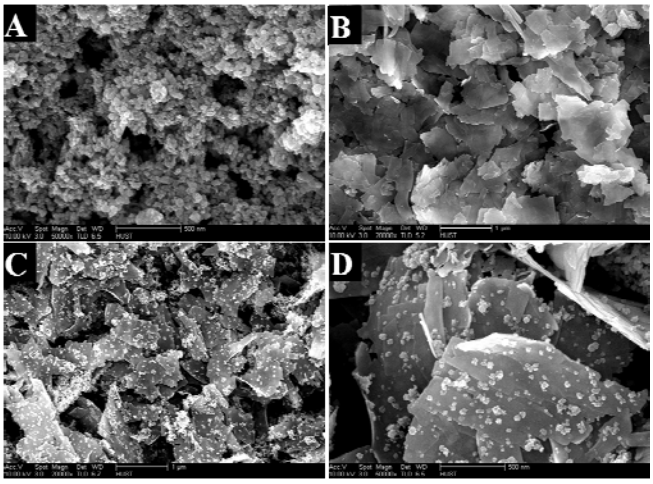

Fig. 2 Typical SEM images of In_2O_3 (A), $La_2Ti_2O_7$ (B) and $In_2O_3/La_2Ti_2O_7$ nanocomposites with a molar ratio of 1.5:1 (C) and (D).

Fig. 3 shows the junction region between In_2O_3 and $La_2Ti_2O_7$ (Fig. 3A) and the morphology of $In_2O_3/La_2Ti_2O_7$ nanocomposite loaded with 1 wt% Pt (Fig. 3B and Fig. 3C). The interplanar distances of 0.291 and 0.278 nm are in good agreement with the d-spacings of the (222) and (002) planes of In_2O_3 and $La_2Ti_2O_7$, respectively. Furthermore, there are obvious transition regions and lattice distortions in the interfacial region between In_2O_3 and $La_2Ti_2O_7$, as shown in the white square frame in Fig. 3A. The lattice distortions are released as the In_2O_3 particles grow.[15, 30] The results suggest that In_2O_3 nanoparticles are uniformly grown onto $La_2Ti_2O_7$ nanosheets and the heterojunction structure between In_2O_3 and $La_2Ti_2O_7$ is successfully formed by this method. For the $In_2O_3/La_2Ti_2O_7$ nanocomposite loaded with 1 wt% Pt, as shown in Fig. 3B and Fig. 3C, a great amount of Pt nanoparticles with a size of ca. 5 nm are uniformly dispersed on the surface of In_2O_3 nanoparticles with a size of ca. 30 nm and $La_2Ti_2O_7$ nanosheets, which are outlined with white circles in Fig. 3B. HRTEM is used to further confirm the deposition of Pt nanoparticles on the surface of In_2O_3, as shown in Fig. 3C. The

interplanar distances of 0.224 and 0.257 nm are in good agreement with the d-spacings of the (111) and (400) planes of Pt and In_2O_3, respectively.

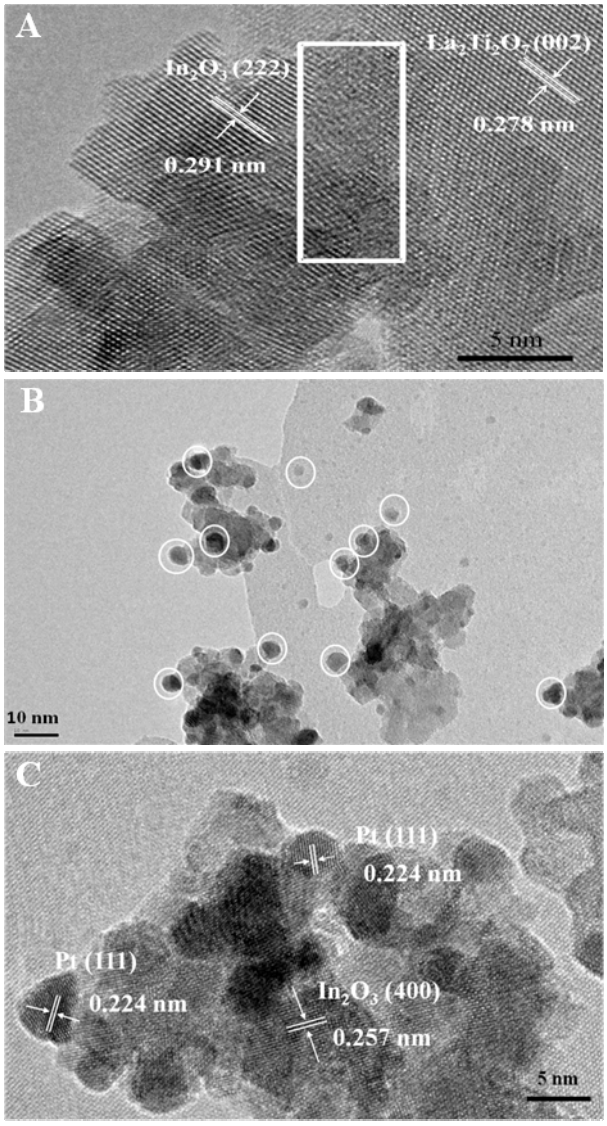

Fig. 3 Typical HRTEM images of $In_2O_3/La_2Ti_2O_7$ nanocomposite with a molar ratio of 1.5:1 (A); $In_2O_3/La_2Ti_2O_7$ nanocomposite loaded with 1 wt% Pt (B) and (C).

3.3. XPS spectra analysis

To confirm the chemical composition and purity of the prepared nanocomposites, the $In_2O_3/La_2Ti_2O_7$ nanocomposite with a molar ratio of 1.5:1 was further studied by XPS analysis. C 1s is used as a reference for correcting the spectra for charge In, La, O and C exist in $In_2O_3/La_2Ti_2O_7$ nanocomposite. The corresponding high-resolution XPS spectra of Ti 2p, In 3d, La In, La, O and C exist in $In_2O_3/La_2Ti_2O_7$ nanocomposite. The corresponding high-resolution XPS spectra of Ti 2p, In 3d, La accumulation. The full spectra (Fig. 4A) show that elements Ti, 3d and O 1s are shown in 4C-4F, respectively. In Fig. 4C, the peaks located at 464.1 eV and 458.7 eV correspond to Ti $2p_{1/2}$ and Ti $2p_{3/2}$, respectively. The splitting between Ti $2p_{1/2}$ and Ti $2p_{3/2}$ is 5.4 eV, indicating a normal state of Ti (IV) in the $In_2O_3/La_2Ti_2O_7$ nanocomposite.[31] For In 3d, shown in Fig. 4D, spin-orbital splitting causes the observed In $3d_{5/2}$ and In $3d_{3/2}$ peaks to have characteristic double peaks centered at binding energies of 444.4 eV and 451.9 eV, respectively, which agrees well with literature values recorded for In (III).[32, 33] Fig. 4E reveals the high-resolution XPS spectra for La 3d. Seven peaks are observed in the La 3d core level spectra, and all of these peaks originate from the spin-orbital splitting of the $3d_{5/2}$ and $3d_{3/2}$ states of La (III).[34, 35] Fig. 4F presents the high-resolution XPS spectra for O 1s. Two oxygen signals are observed at 531.7 and 530.1 eV, which can be attributed to oxygen anions from indium oxide and titanium dioxide, respectively.[36]

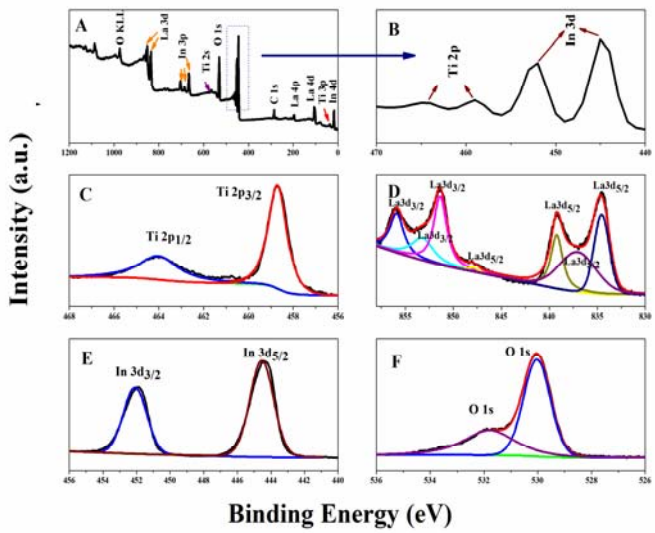

Fig. 4 XPS spectra of an $In_2O_3/La_2Ti_2O_7$ nanocomposite with a molar ratio of 1.5:1. (A) Full spectra; (B) Partial enlarged spectra; (C) Ti 2p; (D) In 3d; (E) La3d and (F) O1s high-resolution XPS spectra.

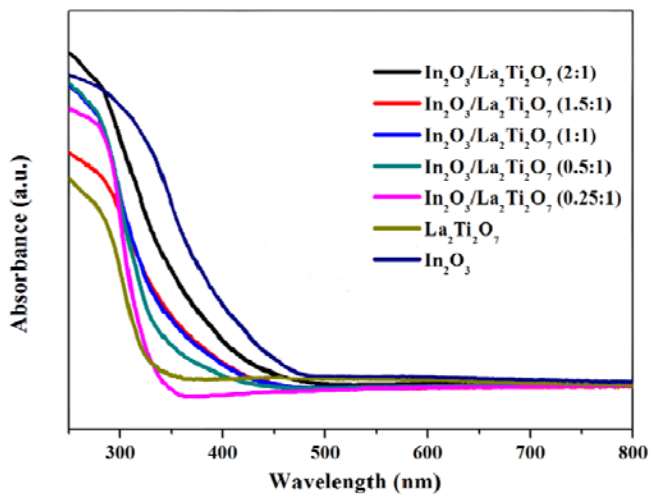

Fig. 5 UV-vis diffuse reflectance spectra of In_2O_3, $La_2Ti_2O_7$ and $In_2O_3/La_2Ti_2O_7$ nanocomposites with different molar ratios.

3.4. UV-vis absorption

Fig. 5 shows the UV-vis diffuse reflectance spectra (DRS) of In_2O_3, $La_2Ti_2O_7$ and several In_2O_3/ $La_2Ti_2O_7$ nanocomposites with different molar ratios. For pure $La_2Ti_2O_7$, the DRS spectrum presents a steep absorption edge at approximately 340 nm, which can be assigned to the intrinsic bandgap absorption of $La_2Ti_2O_7$ (3.8 eV). The DRS spectra of the In_2O_3/ $La_2Ti_2O_7$ nanocomposites are composed of the absorption spectra of In_2O_3 and $La_2Ti_2O_7$, and the absorption boundary red shifts with an increasing amount of In_2O_3 on the $La_2Ti_2O_7$ nanosheets. Meanwhile, the absorption edges do not change obviously, implying that the respective crystal structures of In_2O_3 and $La_2Ti_2O_7$ are retained after the heterojunction forms.

3.5. Photocatalytic water splitting for H_2 evolution activity

The photocatalytic activities of In_2O_3, $La_2Ti_2O_7$ and the $In_2O_3/La_2Ti_2O_7$ nanocomposites with different molar ratios were evaluated by measuring H_2 production from water splitting under 500 W Xe lamp irradiation, as shown in Fig. 6. To improve photocatalytic H_2 production, 1 wt% Pt cocatalyst was loaded onto the photocatalyst surfaces to provide active sites for the reaction. The microstructure of the $In_2O_3/La_2Ti_2O_7$ nanocomposite loaded with 1 wt% Pt is shown in Fig. 3B. As seen from Fig. 6, the photocatalytic H_2 evolution rates over In_2O_3 and pristine $La_2Ti_2O_7$ are only 2.30 and 10.59 μmol h^{-1} g^{-1}, respectively. The H_2 evolution rates are distinctly enhanced by increasing the $In_2O_3/La_2Ti_2O_7$ molar ratio from 0.25:1 to 1.5:1 and subsequently decrease significantly upon further increasing the molar ratio to 2:1. A possible reason for the enhanced photocatalytic H_2 evolution rates when the $In_2O_3/La_2Ti_2O_7$ is changed from 0.25:1 to 1.5:1 is the heterojunction effect existing between In_2O_3 and $La_2Ti_2O_7$. Despite the variation in their activities, all of the above nanocomposites are more active for photocatalytic water splitting than pure In_2O_3 and $La_2Ti_2O_7$, and even perform better than a mechanical mixture of In_2O_3 and $La_2Ti_2O_7$. The $In_2O_3/La_2Ti_2O_7$ nanocomposite with molar ratio of 1:1.5 exhibits the maximum photoactivity (68.14 μmol h^{-1} g^{-1} with an apparent quantum efficiency (AQE) of 0.41 %), which is 29.62 times higher than that of In_2O_3 and 6.43 times that of pure $La_2Ti_2O_7$.

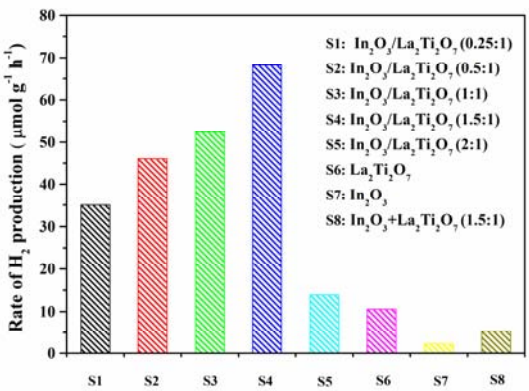

Fig. 6 Photocatalytic H_2 evolution activity of $In_2O_3/La_2Ti_2O_7$ nanocomposites with different molar ratios compared with pure In_2O_3 and $La_2Ti_2O_7$.

Fig. 7 displays the photostability of the Pt (1 wt%)-loaded $In_2O_3/La_2Ti_2O_7$ (1.5:1) photocatalyst, which was investigated in four runs performed over the accumulated course of 8 h. The average H_2 generation rate over Pt (1 wt%) loaded $In_2O_3/La_2Ti_2O_7$ (1.5:1) composite is approximately 56.41 μmol g^{-1} h^{-1} in the first run of 8 h photocatalytic reaction, and then slightly declines to 50.32 μmol g^{-1} h^{-1} in the fourth. The average H_2 generation rate decreases by approximately 10.8 % when the reaction was performed over the nanocomposite for the fourth time, indicating that the photocatalyst has good stability.

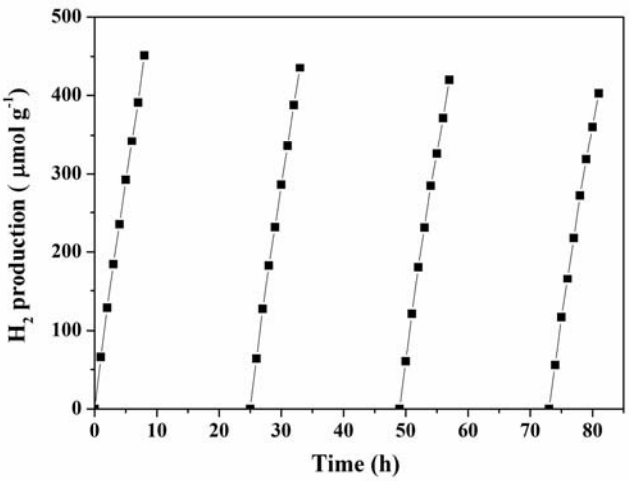

Fig. 7 Time courses of photocatalytic H_2 production over $In_2O_3/La_2Ti_2O_7$ (1.5:1).

3.6. Mechanism of enhanced photoactivity

On the basis of the above experimental results and discussion, we believe that the enhanced photocatalytic activities observed may be attributed to the formation of the heterojunction between In_2O_3 and $La_2Ti_2O_7$ that facilitates interfacial transfer of photogenerated electrons and holes, as shown in Fig. 8. As reported, the CB potentials of In_2O_3 and $La_2Ti_2O_7$ are -0.63 eV and -0.43 eV, respectively.[37-39] Because the CB potential of In_2O_3 is more negative than that of $La_2Ti_2O_7$, the interface band bendings are formed when In_2O_3 contacts with $La_2Ti_2O_7$ resulting in the formation of a built-in potential and a potential barrier of In_2O_3 (Fig. 8A). Under the influence of built-in potential, charges are redistributing for equilibrium, which will make the semiconductors, CH_3HO and H_2O having a same Fermi level. However, the thermodynamic equilibrium will be broken and quasi-Fermi levels are built for In_2O_3 and $La_2Ti_2O_7$ when they are illuminated under solar illumination. Specifically, when the catalysts are under solar irradiation, only the photogenerated electrons in In_2O_3 which have enough energy to stride over the potential barrier can transport to $La_2Ti_2O_7$. The same principle can be applied to the transfer of photogenerated holes from $La_2Ti_2O_7$ to In_2O_3. Therefore, the photogenerated electrons in $La_2Ti_2O_7$ and the holes in In_2O_3 are more easily recombined with each other due to the role of built-in potential and the potential barrier. The accumulated holes in $La_2Ti_2O_7$ and electrons in In_2O_3 can form a photovoltage, resulting in the

anodic and cathodic shifts of the quasi-Fermi level of the $La_2Ti_2O_7$ and In_2O_3 heterojunction (Fig. 8B).[18, 40] In the $In_2O_3/La_2Ti_2O_7$ heterojunction structure, the accumulated holes in $La_2Ti_2O_7$ can be oxidized by sacrificial reagents and the accumulated electrons in In_2O_3 are subsequently transferred to the Pt co-catalyst to generate H_2. Therefore, increasing the amount of In_2O_3 is beneficial for promoting carrier separation in space and hindering charge recombination, leading to a higher rate of photocatalytic H_2 production. However, the decrease in photocatalytic H_2 production at excessive In_2O_3 levels in the composites is likely because the In_2O_3 particles shield the $La_2Ti_2O_7$ from exposure to incident light.

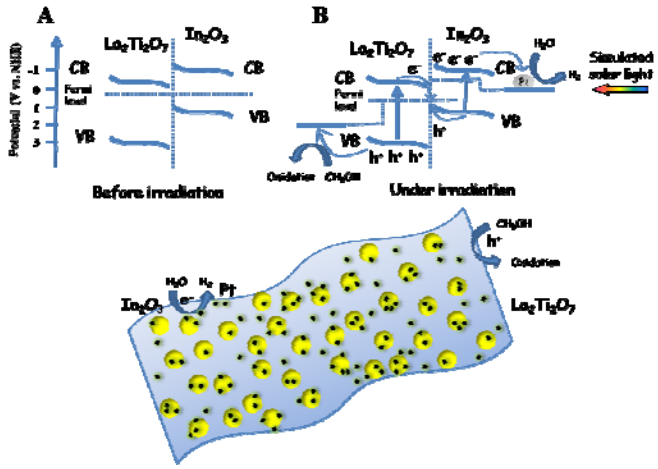

Fig. 8 The proposed photocatalytic H_2 evolution mechanism over $In_2O_3/La_2Ti_2O_7$ nanocomposites under simulated solar light irradiation.

As known, the position of CB and CB edges strongly depends on the preparation methods and experimental condition.[41] Therefore, we measured Mott-Schottky plots for better understanding the intrinsic electronic properties of $In_2O_3/La_2Ti_2O_7$ heterojunction, as shown in Fig. 9. All of $La_2Ti_2O_7$, In_2O_3 and $In_2O_3/La_2Ti_2O_7$ heterojunction show the characteristic behaviors of n-type semiconductors because of the positive slopes of the linear plots. In addition, the flat-band potentials of $La_2Ti_2O_7$, In_2O_3 and $In_2O_3/La_2Ti_2O_7$ heterojunction that measured from Mott-Schottky plots are ca. -0.39, -0.54 and -0.46 eV vs. NHE at pH=7. Because of the different experiment condition, these values have distance with the reported. For n-type semiconductors, donor states and flat band potentials are located just below the bottom of the CB and close to the Fermi level. Therefore, we confirmed $La_2Ti_2O_7$ and In_2O_3 are suitable for water splitting. The location of VB edges can be obtained by DRS and the results are given in Table 1. From the experiment results, we confirmed the CB and VB positions of In_2O_3 are both higher than those of $La_2Ti_2O_7$, the use of an $In_2O_3/La_2Ti_2O_7$ heterojunction would result in an improvement in the efficient separation of photogenerated charge carriers. To further prove that the enhanced photocatalytic H_2 production is due to the formation of the heterojunction rather than simple or random surface contact between the In_2O_3 and $La_2Ti_2O_7$ species, we performed photocatalytic H_2 production and photoluminescence (PL) spectroscopy measurements on In_2O_3+$La_2Ti_2O_7$ (1.5:1), a homogenous, mechanically mixed blend of In_2O_3 and $La_2Ti_2O_7$ with a molar proportion of 1.5:1. The results are shown in Fig. 6 (S8) and Fig. 10. The rate of H_2 production on In_2O_3+$La_2Ti_2O_7$ (1.5:1) (Fig. 6 (S8)) is between $La_2Ti_2O_7$ (Fig. 6 (S6)) and In_2O_3 (Fig. 6 (S7)) and far lower than $In_2O_3/La_2Ti_2O_7$ (1.5:1) (Fig. 6 (S4)). Additionally, the PL spectrum of the In_2O_3+$La_2Ti_2O_7$ (1.5:1) catalyst exhibits a fluorescence increase when compared with $In_2O_3/La_2Ti_2O_7$ (1.5:1), indicating that photogenerated carrier recombination and/or non-radiative recombination is higher than in $In_2O_3/La_2Ti_2O_7$ (1.5:1).[42] Comparison with the mechanical mixture of In_2O_3 and $La_2Ti_2O_7$ indicates that the intimate connection arising from the heterojunction structure and the synergistic effects of the various components promote the spatial separation of the photogenerated carriers and result in the improvement in catalyst photoactivity for H_2 evolution.

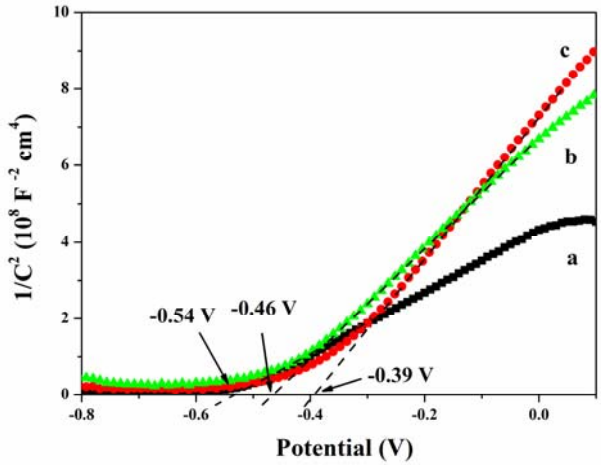

Fig. 9 Typical Mott-Schottky plots of In_2O_3 (a), $In_2O_3/La_2Ti_2O_7$ (1.5:1) (b) and $La_2Ti_2O_7$ (c).

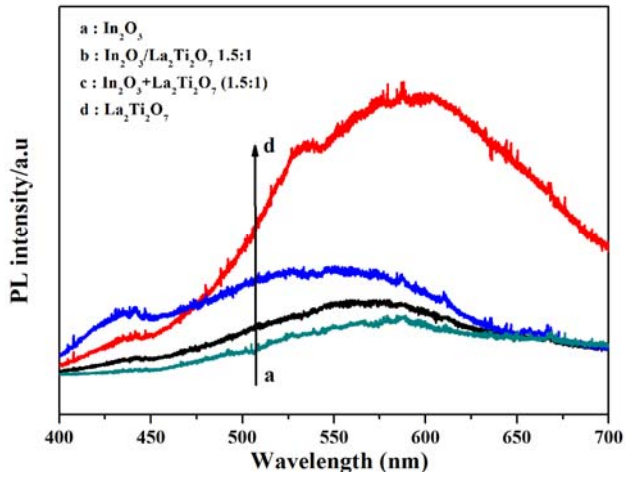

Fig. 10 PL spectra of In_2O_3, $La_2Ti_2O_7$ and $In_2O_3/La_2Ti_2O_7$ nanocomposite and mechanical mixture (In_2O_3 and $La_2Ti_2O_7$) with molar ratio of 1.5:1.

Table 1 The values of Eg, CB and VB edges of $La_2Ti_2O_7$, In_2O_3 and $In_2O_3/La_2Ti_2O_7$ (1.5:1).

	$La_2Ti_2O_7$	In_2O_3	$In_2O_3/La_2Ti_2O_7$ (1.5:1)
Eg	3.65 eV	2.73 eV	3.02 eV
CB edge	-0.39 eV	-0.54 eV	-0.46 eV
VB edge	3.26 eV	2.19 eV	2.56 eV

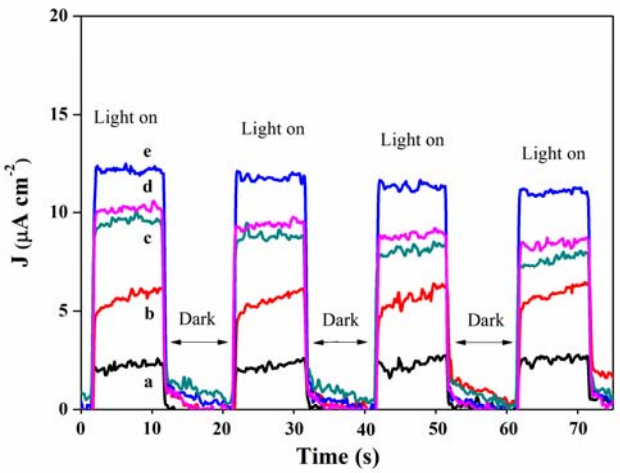

Fig. 11 Transient photocurrent responses of $In_2O_3/La_2Ti_2O_7$ nanocomposites with different molar ratios (0.25:1 (a); 0.5:1 (b); 1:1 (c); 2:1 (d) and 1.5:1 (e)) under simulated solar light in 1 M Na_2SO_4 aqueous solution. Voltage: 0.5 V.

To better understand the influence of $In_2O_3/La_2Ti_2O_7$ molar ratio on the photogenerated carrier separation probability of the $In_2O_3/La_2Ti_2O_7$ nanocomposites, the photocurrent response (J-t) experiments shown in Fig. 11 were performed.[43-46] It can be observed that all of the $In_2O_3/La_2Ti_2O_7$ nanocomposites possess a relatively stable photocurrent response. The photocurrent values of the $In_2O_3/La_2Ti_2O_7$ nanocomposites are enhanced with an increase in the $In_2O_3/La_2Ti_2O_7$ molar ratio from 0.25:1 to 1.5:1 and later decrease on further increase in the molar ratio to 2:1. This changing trend of photocurrent magnitude correlates with the trend in H_2 evolution activity over the nanocomposites. These results indicate that the formed $In_2O_3/La_2Ti_2O_7$ heterojunction is the key to the efficient separation of photogenerated carrier.

4. Conclusions

$In_2O_3/La_2Ti_2O_7$ heterojunction nanocomposites were successfully prepared by a solvothermal method. The investigation of their photocatalytic H_2 production abilities shows that the $In_2O_3/La_2Ti_2O_7$ nanocomposites possess a higher photoactivity for H_2 production than In_2O_3 and pristine $La_2Ti_2O_7$. SEM and TEM reveal that In_2O_3 nanoparticles are grown on and attached to the $La_2Ti_2O_7$ nanosheets surfaces. This combination structure is beneficial for the formation of a heterojunction, which can result in a synergistic combination of In_2O_3 and $La_2Ti_2O_7$ that significantly enhances photogenerated carrier separation and thus improves the rate of photocatalytic H_2 production. The optimal molar ratio of $In_2O_3/La_2Ti_2O_7$ to that end is found to be 1.5:1, and the corresponding H_2 production rate is 68.14 μmol h^{-1} g^{-1} with an apparent quantum efficiency (AQE) of 0.41 %, which is 29.62 times higher than that on pure In_2O_3 and 6.43 times higher than on $La_2Ti_2O_7$. The possible enhancement route and mechanism have also been analyzed. In sum, it has been demonstrated that manipulating the configuration of $In_2O_3/La_2Ti_2O_7$ nanocomposite heterostructures is a quite efficient way to improve photocatalytic H_2 production activity.

Acknowledgements

This work is supported by the National Natural Science Foundation of China (50902056). The authors would like to thank the Materials Characterization Center of Huazhong University of Science and Technology for measurement assistance.

Notes and references

Center for Fuel Cell Innovation, State Key Laboratory of Materials Processing and Die and Mould Technology, School of Materials Science and Engineering, Huazhong University of Science and Technology, Wuhan 430074, China. Fax: + 86 27 87558142; Tel: + 86 27 87558142; E-mail: chibo@hust.edu.cn (B. Chi)

1. A. J. Bard and M. A. Fox, *Accounts of Chemical Research*, 1995, **28**, 141.
2. Y. Amao, *ChemCatChem*, 2011, **3**, 458.
3. J. Barber and B. Andersson, *Nature*, 1994, **370**, 31.
4. S. Dunn, *International Journal of Hydrogen Energy*, 2002, **27**, 235.
5. J. Milliken, F. Joseck, M. Wang and E. Yuzugullu, *Journal of Power Sources*, 2007, **172**, 121.
6. A. Fujishima, K. Honda, *Nature*, 1972, **238**, 37.
7. M. Kitano and M. Hara, *Journal of Materials Chemistry*, 2010, **20**, 627.
8. A. Kudo and Y. Miseki, *Chemical Society Reviews*, 2009, **38**, 253.
9. F. E. Osterloh, *Chemistry of Materials*, 2007, **20**, 35.
10. K. Shimura and H. Yoshida, *Energy & Environmental Science*, 2011, **4**, 2467.
11. D. W. Hwang, H. G. Kim, J. Kim, K. Y. Cha, Y. G. Kim and J. S. Lee, *Journal of Catalysis*, 2000, **193**, 40.
12. H. Kim, D. Hwang, Y. Kim and J. Lee, *Chemical Communications*, 1999, 1077.
13. M. M. Milanova, M. Kakihana, M. Arima, M. Yashima and M. Yoshimura, *Journal of Alloys and Compounds*, 1996, **242**, 6.
14. K. Onozuka, Y. Kawakami, H. Imai, T. Yokoi, T. Tatsumi and J. N. Kondo, *Journal of Solid State Chemistry*, 2012, **192**, 87.
15. K. Li, Y. Wang, H. Wang, M. Zhu and H. Yan, *Nanotechnology*, 2006, **17**, 4863.
16. C. Wu, Y. Zhang, S. Li, H. Zheng, H. Wang, J. Liu, K. Li and H. Yan, *Chemical Engineering Journal*, 2011, **178**, 468.
17. A. Kargar, Y. Jing, S. J. Kim, C. T. Riley, X. Q. Pan and D. L. Wang, *ACS Nano*, 2013, **7**, 11112.
18. N. Liang, J. T. Zai, M. Xu, Q. Zhu and X. F. Qian, *Journal of Materials Chemistry A*, 2014, **2**, 4208.
19. Y. Liu, Y. X. Yu and W. D. Zhang, *The Journal of Physical Chemistry C*, 2013, **117**, 12949.
20. X. Tang, G. Li and S. Zhou, *Nano letters*, 2013, **13**, 5046.
21. H. Zhao, H. Dong, L. Zhang, X. Wang and H. Yang, *Materials Chemistry and Physics*, 2011, **130**, 921.
22. Z. M. Li, P. Y. Zhang, J. G. Li, T. Shao, J. Wang and L. Jin, *Catalysis Communications*, 2014, **43**, 42.
23. P. Liu, J. Nisar, B. Pathak and R. Ahuja, *Physical Chemistry Chemical Physics*, 2013, **15**, 17150.
24. J. Mu, B. Chen, M. Zhang, Z. Guo, P. Zhang, Z. Zhang, Y. Sun, C. Shao and Y. Liu, *ACS Applied Materials & Interfaces*, 2012, **4**, 424.
25. Y. C. Chen, Y. C. Pu and Y. J. Hsu, *The Journal of Physical Chemistry C*, 2012, **116**, 2967.
26. F. Meng, J. Li, Z. Hong, M. Zhi, A. Sakla, C. Xiang and N. Wu, *Catalysis Today*, 2013, **199**, 48.

27. A. A. Ismail and D. W. Bahnemann, *The Journal of Physical Chemistry C*, 2011, **115**, 5784.
28. M. S. Zhu, Z. Li, B. Xiao, Y. T. Lu, Y. K. Du, P. Yang and X. M. Wang, *ACS Applied Materials & Interfaces*, 2013, **5**, 1732.
29. Q. Xiang, J. Yu and M. Jaroniec, *Journal of the American Chemical Society*, 2012, **134**, 6575.
30. S. W. Cao, X. F. Liu, Y. P. Yuan, Z. Y. Zhang, Y. S. Liao, J. Fang, S. C. J. Loo, T. C. Sum and C. Xue, *Applied Catalysis B: Environmental,* 2014, **147**, 940.
31. S. Bouattour, A. M. Botelho do Rego and L. F. Vieira Ferreira, *Materials Research Bulletin*, 2010, **45**, 818.
32. J. Mu, B. Chen, M. Zhang, Z. Guo, P. Zhang, Z. Zhang, Y. Sun, C. Shao and Y. Liu, *ACS Applied Materials & Interfaces*, 2011, **4**, 424.
33. C. Chen, D. Chen, X. Jiao and S. Chen, *The Journal of Physical Chemistry C*, 2007, **111**, 18039.
34. M. Sunding, K. Hadidi, S. Diplas, O. Løvvik, T. Norby and A. Gunnæs, *Journal of Electron Spectroscopy and Related Phenomena*, 2011, **184**, 399.
35. M. Yang, L. Huo, H. Zhao, S. Gao and Z. Rong, *Sensors and Actuators. B: Chemical*, 2009, **143**, 111.
36. V. Bessergenev, R. Pereira, M. Mateus, I. Khmelinskii, D. Vasconcelos, R. Nicula, E. Burkel, A. Botelho do Rego and A. Saprykin, *Thin Solid Films*, 2006, **503**, 29.
37. Z. M. Li, P. Y. Zhang, J. G. Li, T. Shao, J. Wang and L. Jin, *Catalysis Communications*, 2014, **43**, 42.
38. Y. C Chen, Y. C. Pu and Y. J. Hsu, *The Journal of Physical Chemistry C*, 2012, **116**, 2967.
39. D. W. Hwang, H. G. Kim, J. S. Lee, J. Kim, W. Li and S. H. Oh, *The Journal of Physical Chemistry C*, 2005, **109**, 2093.
40. M. T. Mayer, C. Du and D. W. Wang, *Journal of the American Chemical Society*, 2012, **134**, 12406.
41. Y. Xu and M. A. A. Schooene, *American Mineralogist*, 2000, **85**, 543.
42. E. C. Carroll, O. C. Compton, D. Madsen, F. E. Osterloh, and D. S. Larsen, *The Journal of Physical Chemistry C*, 2008, **112**, 2394.
43. C. Y. Zhai, M. S. Zhu, Y. T. Lu, F. F. Ren, C. Q. Wang, Y. K. Du and P.Yang, *Physical Chemistry Chemical Physics*, 2014, **16**, 14800-14807.
44. M. S. Zhu, Y. K. Du, P. Yang and X. Wang, *Catalysis Science & Technology*, 2013, **3**, 2295.
45. S. J. Hu, L. C. Jia, B. Chi, J. Pu and J. Li, *Journal of Power Sources*, 2014, **6**, 304.
46. M. S. Zhu, Z. Li, Y. Q. Du, Z. G. Mou and P. Yang, CHEMCATCHEM, 2012, **4**, 112.